Ion flow measurements and plasma current analysis in the Irvine Field Reversed Configuration

W. S. Harris, E. Trask, T. Roche, E. P. Garate, W. W. Heidbrink, and R. McWilliams
Department of Physics and Astronomy, University of California, Irvine, California 92697, USA

(Received 10 April 2009; accepted 28 October 2009; published online 20 November 2009)

Measurements of the Doppler shift of impurity lines indicate that there is an ion flow of ~7 km/s in the Irvine Field Reversed Configuration. A charge-exchange neutral particle analyzer shows the peak energy is below the 20 eV minimum detectable energy threshold, which is in agreement with the spectroscopic data. By evaluating the collision times between the impurities and hydrogen, the dominant plasma ion species, it is concluded that the ions rotate with an angular frequency of $\sim 4 \times 10^4$ rad/s. Estimates of the ion current in the laboratory frame indicate it is one to two orders of magnitude larger than the measured plasma current of 15 kA. Electron drifts are expected to cancel most of the ion current based on the measured magnetic fields and calculated electric fields. © *2009 American Institute of Physics*. [doi:10.1063/1.3265961]

I. INTRODUCTION

The stability of field reversed configurations (FRCs) has shown promise over the years as a potential fusion reactor.[1] It has been postulated[2] that the stability can be attributed, in part, to large orbit ions. These orbits, called betatron orbits,[3] have a gyroradius that is comparable to the major radius of the plasma and travel in the direction of the plasma current. The first step in determining whether ions in betatron orbits are the dominant current carriers is to find out whether ions or electrons are carrying the current.

Past experiments have successfully measured ion impurity flow in a FRC.[4–6] The focus of these measurements, performed on the Field Reversal Experiment (FRX-C) and the FRC Injection Experiment (FIX), has primarily been to study the effect of a stabilizing quadrupole field.[4,5] Ion flow has also been observed in the Swarthmore Spheromak Experiment (SSX) resulting in drift velocities similar to those presented here.[7] The incorporation into an overall ion current density was not shown, until recently in the Tokyo University Spherical Torus (TS-3) merging device.[6] The TS-3 experiment used the ion flow measurement in conjunction with electron density measurements using an electrostatic probe to arrive at the ion current density. The total current density was obtained from a two dimensional magnetic probe array.

The goal of the present work is to evaluate the contribution that ions make to the total plasma current in the Irvine Field Reversed Configuration (IFRC). Although it does not answer the question of what ion orbits are present in the FRC, it helps assess the role ions play in stability. Visible emission spectroscopy is performed on H, He, C^+, Ar^+, and Kr^+ in IFRC and Doppler shifts are measured to confirm that flow is occurring in the ion's diamagnetic direction. Neutral particle analysis is performed on IFRC and indicates that the peak drift energy is less than 20 eV, which is below the minimum detectable energy for the diagnostic. A second harmonic interferometer (SHI) is used for line integrated density measurements[8] and magnetic field profiles are measured and used as a fit to an equilibrium model to obtain the density distribution. These measurements were sufficient to estimate the ion contribution to the total plasma current.

This paper presents measurements that indicate ion flow in the direction of the diamagnetic current. Section II describes the IFRC and the diagnostics used for the presented data. In Sec. III, data from all diagnostics are presented. A discussion of the various data is presented along with an estimate of the ion contribution to the total current in Sec. IV. Future work and conclusions are described in Sec. V.

II. THE IRVINE FRC

A. Machine overview

The IFRC is a coaxial device (Fig. 1) that is similar to the coaxial slow source.[9] The two concentric solenoidal coils are both pulsed *L-C* circuits with variable time delays between them and the plasma source. The plasma is created by a 12 kV discharge (lasting at 10–20 μs) across 16 cable guns—eight on each side of the confinement region. The cable guns are RG-8 coaxial cables with a polyethylene insulator whose tips have been bored out creating a 45° cone. As the arc travels across the surface of the insulator, the plasma is ejected from the guns through the $J_r \times B_\theta$ force. Polyethylene consists of long chains of the ethylene molecule (C_2H_4), so we expect and observe a plasma with hydrogen as the dominant ion species along with a significant portion of carbon.

An axial ($\hat{z}$) background magnetic field, typically around 250 G, is generated by a 110 μs rise time capacitive discharge pulsing of 16 kA through the outer (limiter) coil. When the 14 kA capacitive discharge flows through the inner (flux) coil, creating a peak field of 0.4 T, a toroidal electric field is generated through Faraday's law. This induces a diamagnetic current in the plasma which reverses the magnetic field at the inner radii and establishes an equilibrium.

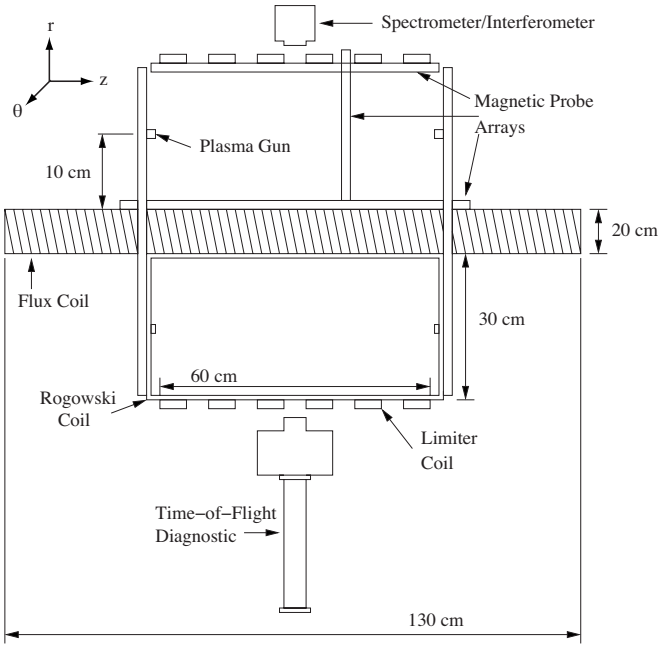

FIG. 1. Coil geometry and principal diagnostics (time-of-flight diagnostic not to scale).

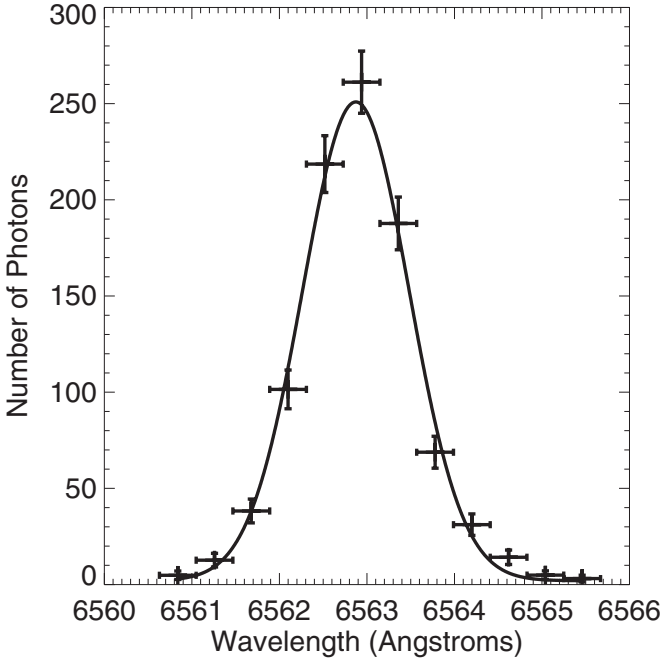

FIG. 2. Gaussian fit performed over an average of five shots looking at H_α at $t=60$ μs. Here, $\Delta\lambda=0.6$ Å and $\lambda_0=6562.9$ Å.

B. Diagnostics

A three-component magnetic probe array consisting of 16 coils spaced nonuniformly (between 1 and 3 cm spacing) is inserted into the plasma to measure the radial dependence of the magnetic field (B_r, B_θ, B_z). The data from the $\hat{z}$-component of the probes are used to fit the free parameters described in Sec. IV D to determine the plasma equilibrium. This array is movable and can be placed at any of 12 positions between the limiter coil straps. In the space between the flux coil, limiter coil, and plasma guns, a Rogowski coil borders the entire confinement region and measures the total plasma current. A charge-exchange neutral particle analyzer[10] is used to measure the energies of the neutrals emitted from the plasma. Error bars on all diagnostics are dominated by shot to shot variation and are computed by the standard deviation between five shots at a minimum.

Visible emission spectroscopy is performed using a SPEX 1702 Czerny–Turner spectrometer with 1800 grooves/mm. A tangential line of sight is used by the spectrometer for both the Doppler shift and electron temperature measurements. The entrance and exit slits of the spectrometer are 30 and 680 μm, respectively. The exit slit is magnified by a factor of 23 using a pair of cylindrical lenses with focal lengths of 6.4 and 150 mm in order to be imaged onto a 16 channel photomultiplier tube (PMT) array (Hamamatsu R5900U-20-L16). The PMT array allows multiple wavelengths to be recorded versus time using three Tektronix TDS 2014 digital storage oscilloscopes. The PMT channel spacing of 1 mm corresponds to a wavelength separation of 0.45 Å after magnification. The instrumental broadening was measured to be 0.3 Å using a hydrogen discharge lamp. Presently, 12 channels are in use giving an observed wavelength range of 4.62 Å.

In order to measure a Doppler shift, the mapping from PMT channel number to wavelength must be accurately known. The lens setup on the spectrometer is very sensitive to daily temperature fluctuations and so the mapping was recalibrated before and after each data run. For hydrogen, this is accomplished by using a hydrogen lamp. For all other lines, the hydrogen lamp is first used as a reference to get close to the desired wavelength. Then the average line wavelength λ_0, corresponding to no Doppler shift, is found by taking the average of the peak wavelengths when looking cocurrent and countercurrent during different plasma shots. Once the mapping of channel number to wavelength is accomplished, the Doppler shift and broadening are determined by Gaussian fitting.

A least-squares fit of a Gaussian distribution is applied to the observed spectra so that the average wavelength and spread can be calculated as a function of time. A sample spectrum from a standard IFRC shot looking at the H_α line is shown in Fig. 2 along with its corresponding Gaussian fit. As shown in the data, the spectrometer raw signal is converted to a number of photon counts N by dividing the measured current by the anode gain (10^6). The $\sqrt{N}$-errors are used for the weights in computing the Gaussian fit. Error bars for temperature and drift velocity measurements are obtained from the statistical deviation of the resulting Gaussian fit parameters between multiple shots.

A SHI (Ref. 8) is used to measure the line-integrated plasma density throughout the plasma discharge. The line of sight passes through a chord whose minimum radius is 10 cm from the flux coil. The data from this diagnostic are used for normalization of the calculated density profiles in Sec. IV D. In addition, local density measurements are made using an ion saturation current probe.

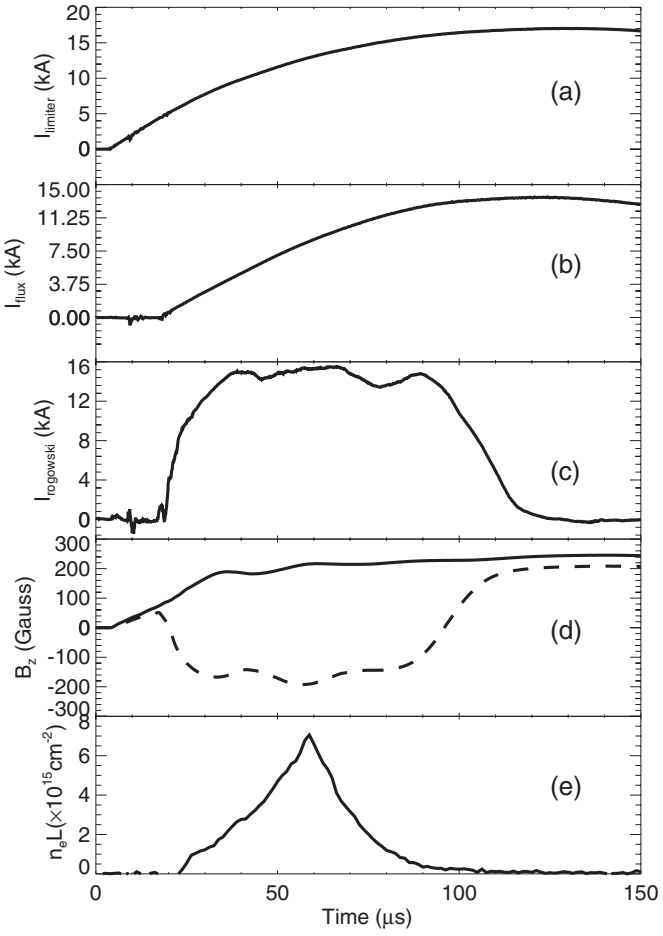

FIG. 3. Current through the (a) limiter coil, (b) flux coil, and (c) total plasma current. Axial magnetic field (d) at the midplane on the outermost radius (solid) and innermost radius (dashed). Line integrated density (e) measured on a similar discharge. Standard plasma shot with 5.4 kV on the flux coil, 1.4 kV on the limiter coil, and 16 kV on the plasma guns.

III. EXPERIMENTAL DATA

The timing of the magnetic fields in IFRC is shown by the current traces in Fig. 3. Figure 3(a) shows the current that provides the background magnetic field through the limiter coil; the flux coil current, delayed about 13 μs, is shown in Fig. 3(b). Rogowski coil measurements show the plasma current starts to rise when the plasma guns fire about 5 μs after the limiter fires, and peaks at 15 kA. The magnetic field measured at the flux coil (innermost) and limiter coil (outermost) radii in Fig. 3(d) shows typical field reversal of $\pm$200 G and a lifetime of 80 μs. The line integrated electron density for a typical shot is shown in Fig. 3(e). As observed in these traces, the plasma current starts to drop as the flux coil approaches its peak. It is not clear whether the lifetime is restricted by the rise time of the flux coil or density decay since the line integrated density starts to decay much earlier than the current; however the radial magnetic probe data (below) suggest the former. Radial magnetic probe measurements show the null surface moving inward and out of the interferometer's line of sight during this time, which is consistent with the observed peaked profile. Viewing port limitations restrict the interferometer chord to the present location.

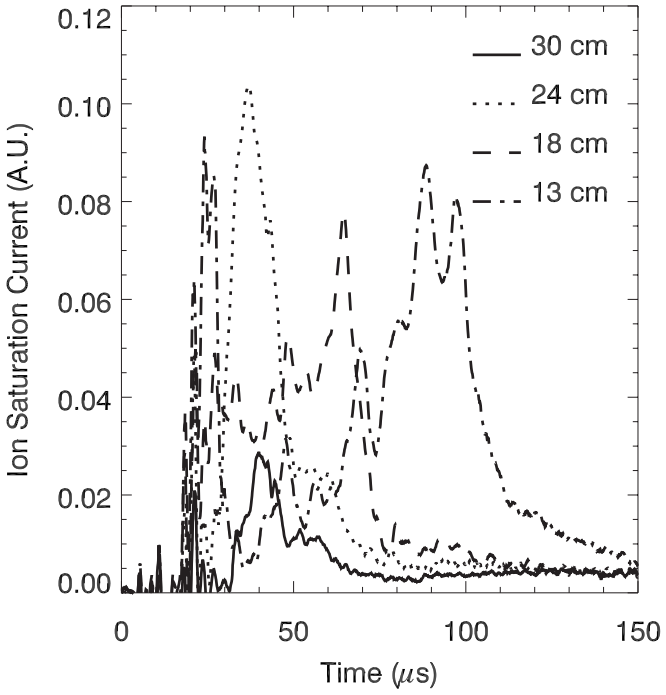

FIG. 4. Ion saturation current at various radii with standard charging parameters.

As a comparison to the interferometer's time evolution, measurements at several radial locations from the ion saturation current probe are shown in Fig. 4. Around 20 μs the flux coil fires and noise is picked up by the probe. The outermost location (solid) peaks early at around 40 μs and for the most part is smaller than all of the other positions throughout the discharge. At the innermost position (dashed-dot), the signal peaks around 90 μs indicating that the plasma ring is contracting. Looking at the intermediate positions, the density profile peaks at ~24 cm at 40 μs and passes through 18 cm at 60 μs. The contraction of the plasma inferred from these ion saturation current measurements is consistent with the interferometer signal, which falls rapidly after 60 μs because the plasma column has contracted beyond the 20 cm minimum radius of its sightline.

A radial array of magnetic probes oriented in the axial direction is used to map the magnetic structure within the plasma. The resulting data are shown in Fig. 5 with nine probes left out of the figure for clarity. Numerical integration of the magnetic probe signals results in an error up to $\pm$5% over the FRC lifetime. The null radius where B=0 is found by interpolating the radial probe data. Theoretically (Sec. IV D), the peak density is centered near the null surface, so this estimate of the null radius provides an estimate of the extent of the current ring. The radial array also measures the toroidal magnetic field. Transient toroidal fields with a root mean square value that is 20% of the peak reversed B_z field are observed in most discharges.

Raw data from the charge-exchange neutral particle analyzer are shown in Fig. 6. The observed neutral flux raw signal peaks at ~60 eV. After taking into account the energy dependent detector sensitivity and charge-exchange cross section, these data indicate that the peak toroidal drift energy

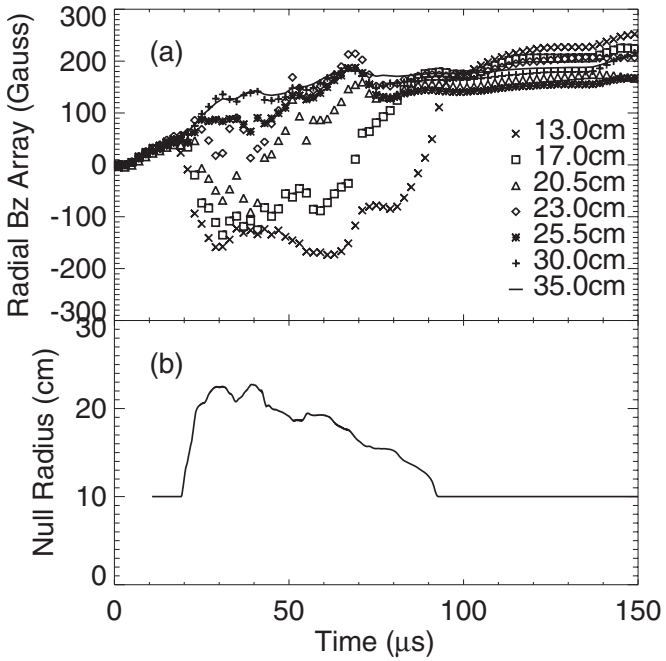

FIG. 5. (a) Radial magnetic field profile at the midplane for a typical shot. Only seven probes are shown for clarity. (b) The interpolated null surface vs time.

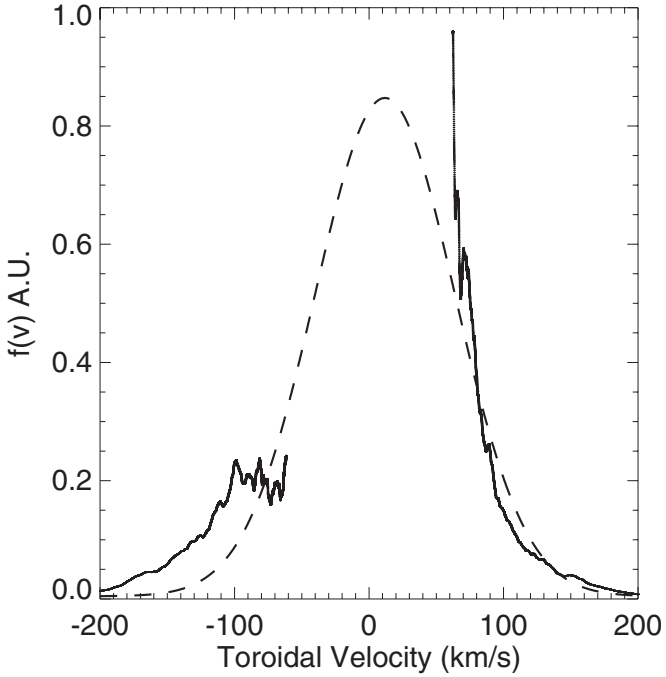

FIG. 7. Neutral flux measurements looking in the cocurrent ($v<0$) and countercurrent ($v>0$) directions (solid). Cartoon indicating that peak of data lies below minimum detectable energy (dashed). Data shown are taken at $t=63$ μs for a typical shot.

of the detected neutrals is less than 20 eV (30 km/s), which is the low energy cutoff for the diagnostic. Data corrected for the energy dependence of the charge-exchange cross section and detector sensitivity are shown for typical charging parameters in Fig. 7. The data shown are obtained by averaging five shots with the detector looking in the cocurrent direction, so that detected neutrals ($v<0$) must be traveling in the countercurrent direction, and repeated with the detector facing in the countercurrent direction ($v>0$). Asymmetry of the data around $v=0$ suggests a net flow in the cocurrent direction. The corrected distribution increasing as v approaches the energy cutoff indicates that the average flow of neutrals must be less than 30 km/s, which is in agreement with the spectroscopic data shown below.

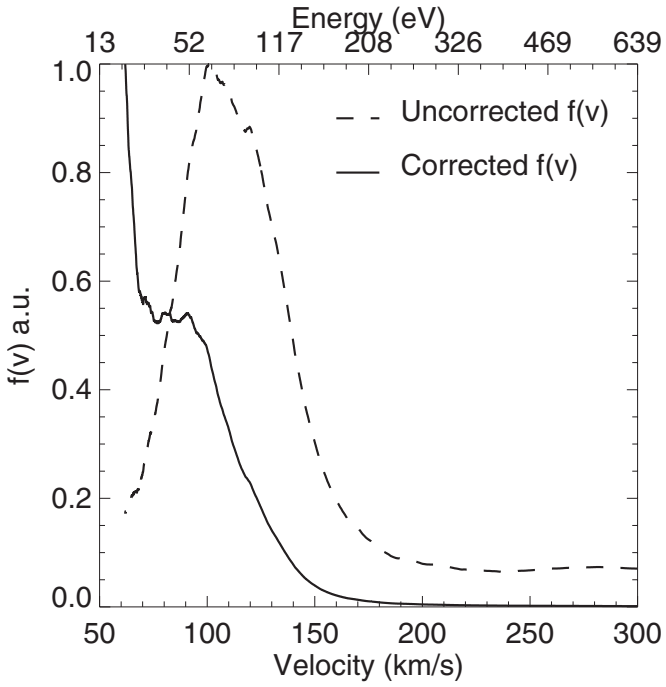

FIG. 6. Charge-exchange neutral particle velocity distribution uncorrected (dashed) and corrected (solid) for detection efficiency and charge exchange cross section energy dependence. Time averaged over 45–90 μs for a standard plasma shot.

Visible emission spectroscopy is performed on hydrogen and carbon (products from the plasma source), as well as helium, argon, and krypton impurities in order to measure the drift velocity at energies less than the charge-exchange analyzer's cutoff. The impurities are introduced individually in different IFRC discharges by filling a plenum attached to the plasma vessel by a needle valve, and opening the valve until background pressures resulting in measurable line emissions (>20 mV) are reached. Table I summarizes the observed lines. Injection of the impurities does not have a noticeable effect on the plasma discharge. Plasma current traces and magnetic probe signals measured with the addition of impurities fall within the shot to shot variation in those measured without impurities. Electron density measurements are not available for the IFRC discharges with impurities because the interferometer was removed from the experiment prior to the completion of the spectrometer.

A Gaussian fit of the argon line is shown for observation in the countercurrent direction in Fig. 8. As shown in the figure, the fitted Gaussian (solid) is blueshifted in comparison to the unshifted line (dashed). The Doppler shifts of the argon line for two typical shots looking in opposite tangential directions are shown in Fig. 9. The data shown are the mean channel number resulting from the Gaussian fit de-

TABLE I. Lines analyzed.

Species	H	He	C	Ar	Kr
Ionization	I	I	II	II	II
Transition	$2p$-$3d$	$1s2p$-$1s3d$	$2s^23s$-$2s^23p$	$3s^23p^44s$-$3s^23p^44p$	$4s^24p^45s$-$4s^24p^45p$
Wavelength (Å)	6562.85	5875.62	6578.05	4879.86	5681.90
Fill pressure (Torr)	⋯	1.1×10^{-4}	⋯	1.6×10^{-5}	1.3×10^{-5}

scribed in Sec. II B. It is clear that by looking in the opposite tangential direction, the Doppler shift is reversed indicating a correlation between the direction of observation (cocurrent and countercurrent) and direction of Doppler shift (redshift and blueshift). This is in agreement with Fig. 7 which shows an asymmetric distribution weighted toward neutrals rotating in the cocurrent direction. For the data shown in Fig. 10, the Doppler shift from the cocurrent observation direction was subtracted from the countercurrent direction and divided by two showing the net impurity ion flow in the direction of the plasma current. The measured Doppler shifts for ArII, KrII, and CII correspond to a drift velocity of 5–7 km/s during the stable FRC time period.

The measured energy spread or effective temperature was determined by fitting the spectrum to a Gaussian distribution, and converting the wavelength spread into a Doppler broadened temperature after correcting for the instrumental broadening. Figure 11 shows the calculated effective temperatures. Although hydrogen and helium appear to have a temperature in the range of 5–10 eV, the ion species peak around 100 eV. This difference in energy spread could be a line integral effect due to the radial electric field calculated in Sec. IV D which only influences the ions.

The electron temperature can be estimated by the emissivity ratio of different spectral lines in hydrogen.[11] The ratio of H_α to H_β emission is used for this analysis, and the resulting data are shown in Fig. 12. As calculated using this method, the electron temperature is in the range of 2–4 eV through the majority of the discharge.

IV. DISCUSSION

In Sec. III, the data indicate that there is a Doppler shift of impurity lines in the direction of the plasma current. This is discussed in Sec. IV A along with its agreement with the neutral particle measurements. The determination of the electron temperature is discussed in Sec. IV B along with its validity. Section IV C shows a calculation of the density profile from magnetic probe measurements using pressure balance. A theoretical equilibrium is presented and a density profile resulting from fitting the equilibrium magnetic fields to the experimental data is in Sec. IV D. The process by which the ion contribution to the plasma current is determined is presented and the calculations are carried out in Sec. IV E. These ion currents are compared with the 15 kA total plasma current and the electron component is evaluated.

A. Ion drift measurements

As shown in Fig. 10, there is an overall drift for the observed ion species that peaks in the range of 5–7 km/s. This is consistent with what is expected in a rigid rotor distribution-all species should rotate at the same velocity provided that the collisionality between them and/or the bulk plasma is sufficiently high compared with the lifetime of the plasma. When viewed from the opposite tangential direction, the resulting Doppler shift is in the opposite direction, as expected for a rotating plasma.

The Coulomb collisional (ion-ion) relaxation time[12] for a stationary test particle to equilibrate with a rotating plasma has been calculated for the standard plasma condition in IFRC. For singly ionized carbon, the relaxation time is in the range of 2–8 μs for the plasma density between 100% and 25% of its peak value ($\sim1.5\times10^{15}$ cm^{-3}, as determined in Sec. IV D, and an ion temperature of 5eV). Using the same plasma parameters, the relaxation time is in the range of 7–27 μs for singly ionized argon. For krypton, the relaxation time for the same parameters is 15–55 μs. The krypton estimate is consistent with the ~50 μs delay in acceleration relative to argon and carbon in Fig. 10. The same reasoning suggests that the argon acceleration should lag car-

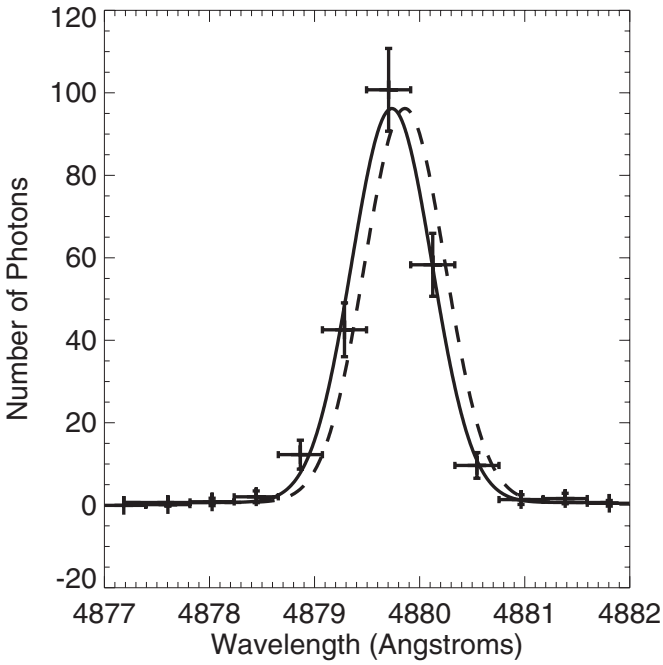

FIG. 8. Argon data (+) with a Gaussian fit (solid) observed in the countercurrent direction showing a blueshift. The unshifted Gaussian (dashed) is shown for comparison.

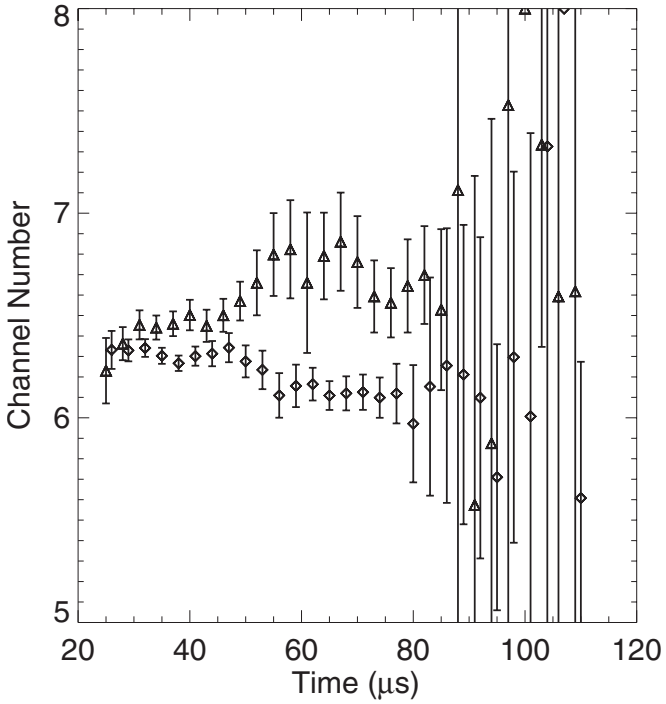

FIG. 9. Gaussian fit giving the mean PMT channel number observed in the cocurrent (△) and countercurrent (◇) directions. Error bars are calculated from the shot to shot variation in the discharges.

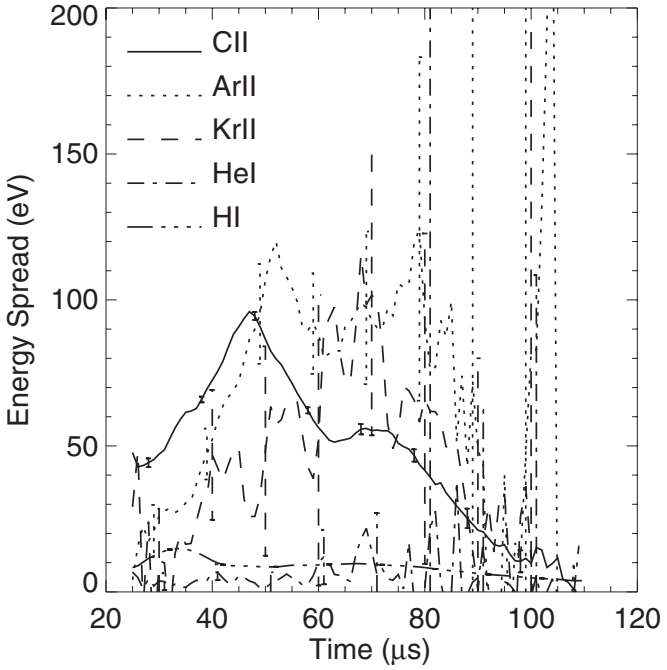

FIG. 11. Effective temperatures for observed spectral lines: hydrogen (dashed-dot-dot-dot), helium (dashed-dot), carbon (solid), argon (dotted), and krypton (dashed).

bon; however this is not observed. Drag on the electron fluid may also play a role since the electron-ion collisionality is larger for smaller masses.

Neutral hydrogen spectroscopy, however, shows no Doppler shift. It is possible that this is due to a neutral density population that is sparse within the core of the plasma, and most dense on the edge. In this picture, the majority of light from hydrogen emission occurs at the edge where there is little or no rotation. Feasibility of this explanation is examined by considering the effective mean free path l_i for the ionization of hydrogen in a plasma. The average cross section $\langle \sigma v \rangle$ for electron impact ionization of hydrogen as a function of electron temperature[13] can be used in conjunction

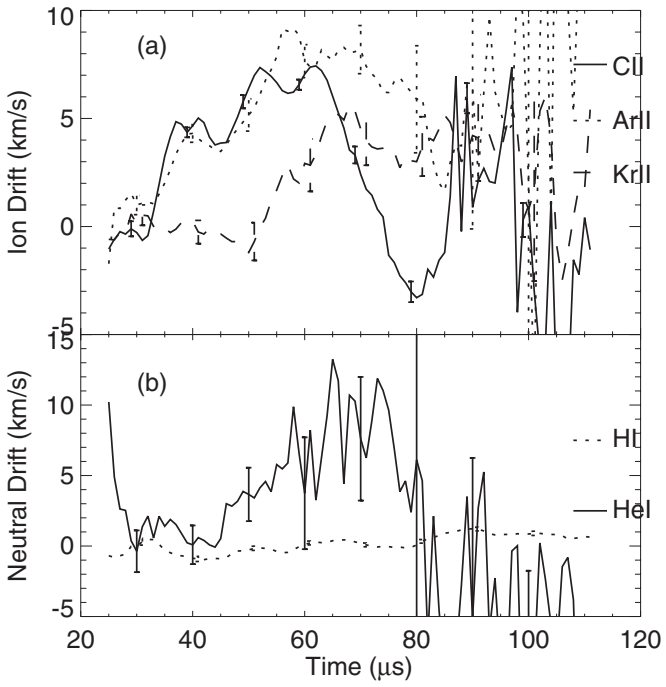

FIG. 10. Average Doppler shift for observed spectral lines. Ion lines shown in (a) are carbon (solid), argon (dotted), and krypton (dashed). Neutral emission lines (b) are helium (solid) and hydrogen (dotted).

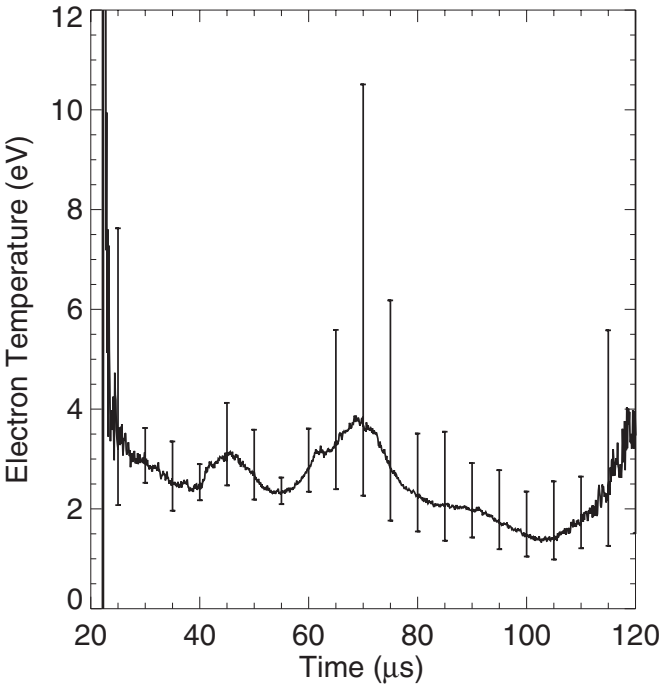

FIG. 12. Electron temperature as determined by the ratio of H_α to H_β. Error bars from statistical deviation of intensity between multiple shots.

with the electron density to estimate the mean free path, $\ell_i \simeq 1/n_e\sigma \simeq 3$ cm. Based on this analysis, the majority of neutrals will be ionized upon penetrating at ~3 cm of the plasma and line radiation occurs primarily at the edge.

The helium neutrals appear to have an average drift in the same range as the impurities. The signal to noise ratio for the helium line, however, was at most ~2 during the stable portion of the discharge, resulting in poor Gaussian fitting and large error bars in determining the Doppler shift. In addition, the time response for the drift measured by helium appears to lag behind carbon and argon.

The data from the charge-exchange analyzer indicate that the peak neutral flux emitted from the plasma is below the 20 eV minimum measurable energy of the detector, resulting in the observed high energy tail. This is in agreement with the spectrometer since hydrogen, if rotating at 7 km/s like the impurities, has an energy of 0.25 eV. It is unclear whether the observed neutrals originate from the core or the edge. Previous experiments[14] show the electron temperature to be uniform across the radial extent of the plasma, and the ions are expected to have a similar profile due to high collisionality. A Gaussian fit to the data gives a temperature of 14 eV.

B. Electron temperature

For the method of determining the electron temperature in Fig. 12 from a line ratio to be valid, the following requirements must be satisfied:[11] electrons satisfy a Maxwellian velocity distribution, the plasma is optically thin, and the plasma is in coronal equilibrium. The Maxwellian distribution is justified since the electron-electron Coulomb collision time is ~25 ps while the plasma lifetime is 80 μs. Although opacity measurements have not been performed, it is a reasonable assumption that the plasma is optically thin based on the fact that ion Doppler shifts are observed, which presumably originate from the plasma core. The coronal equilibrium condition has been evaluated as follows: the source rates for neutrals $n_i\langle\sigma_{\mathrm{rec}}v\rangle$ and electrons $n_n\langle\sigma_{\mathrm{ion}}v\rangle$ through recombination and electron-impact ionization have been compared with the lifetime of the plasma. Although the exact neutral hydrogen density is not known, assuming $n_n \approx 0.01 n_i$ and an electron temperature of 3 eV (which is the resulting temperature from the model in question) results in time scales for the corresponding rates of 2 ms and 200 μs for sourcing neutrals and electrons, respectively. Since the lifetime of the plasma is typically 80 μs, the coronal model can be employed for electron temperature measurements to a reasonable approximation.

Electron temperature profiles have been shown[14] to be uniform inside the separatrix. Based on this, calculations involving the electron temperature such as the pressure balance condition assume that the temperature is uniform throughout the plasma.

It should also be noted that although the electron temperature is far below the ionization energy for hydrogen, it is still reasonable to assume a large degree of ionization. A calculation of the ionization ratio N_+/N_0 from the Saha equation gives nearly 10^4 for $T_e=2$ eV. In addition, since the plasma is formed at each of the 16 plasma gun sources (each charged to 16 kV), the temperature presumably cools as the plasma expands to fill the vessel. Because of this, the electron temperature measured in the main chamber is not the limiting factor in the ionization process.

C. Density profile from pressure balance

The magnetic probe data have been used to construct the density distribution by using the pressure balance condition

$$\nabla(p + B^2/2\mu_0) = (B\cdot\nabla)B/\mu_0, \tag{1}$$

where $B=B(r,z)$. It should be noted that for the measured magnetic fields, the right hand side is within an order of magnitude of the left hand side of Eq. (1), so it cannot be approximated to zero as in other cases. Looking at the radial component and integrating to obtain the density as a function of r and z gives

$$n(r,z) = \frac{1}{\mu_0 T}\left[\int\left(B_r\frac{\partial B_z}{\partial r} - \frac{B_\theta^2}{r}\right)dr - \frac{1}{2}(B_\theta^2 + B_z^2)\right], \tag{2}$$

where the temperature T is assumed to be constant throughout the plasma. The density profile obtained from this is valid up to an arbitrary constant, which is determined by choosing the density at the minimum point along each radius to be zero. Thus, a lower bound on the density is obtained using this method.

The density appears to increase at the radial boundaries using this method. This is presumably because of eddy currents generated in the coils which cancel out the magnetic fields near them, which results in local magnetic field maxima within a few centimeters of the coils. By applying the condition that the density goes to zero at the boundaries, the profile more closely resembles what has been measured by a Langmuir probe in Sec. IV D. The calculated density distribution during a stable portion of the discharge is shown in Fig. 13.

D. Equilibrium fitting

The rigid rotor distribution function

$$f_j(r,z,\vec{v}) = \left(\frac{m_j}{2\pi T_j}\right)^{3/2} n_j(r,z)\exp\left\{-\frac{m_j}{2T_j}|\vec{v} - \omega_j\times\vec{r}|^2\right\} \tag{3}$$

has been used to arrive at the equilibrium density and electromagnetic fields in a FRC by solving the Vlasov–Maxwell equations.[15] The physical interpretation of Eq. (3) is that the particles rotate uniformly with an angular frequency ω_j.

A one-dimensional (1D) solution[15] of the momentum equation for a rigid rotor gives a density profile

$$n_i(r) = \frac{n_{i0}}{\cosh^2\left(\dfrac{r-r_0}{r_0\Delta r}\right)}, \tag{4}$$

where n_{i0} is the peak density at r_0 and Δr is an effective radial thickness. This density profile is used for calculations in Sec. IV E. The radial dependence of the magnetic field from this equilibrium model is

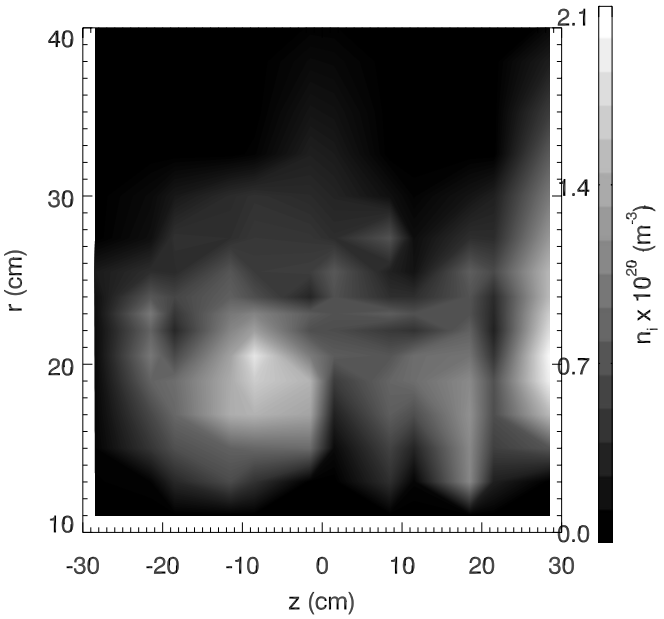

FIG. 13. Density profile obtained from pressure balance at $t=60$ μs while plasma is stable with the condition that the density goes to zero at the boundary.

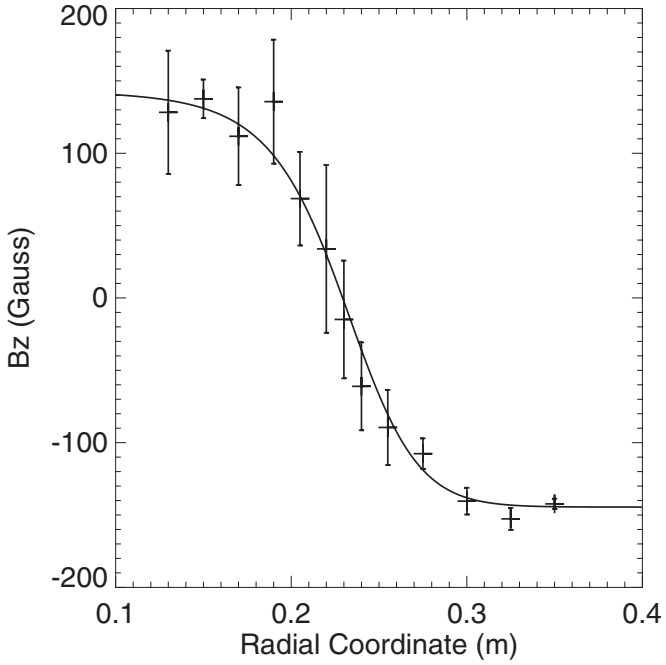

FIG. 14. Equilibrium fit to data for a typical shot to obtain equilibrium parameters at $t=40$ μs.

$$B_z(r) = -B_0\left[1+\sqrt{\beta}\tanh\left(\frac{r^2-r_0^2}{r_0\Delta r}\right)\right], \tag{5}$$

where B_0 is the externally applied magnetic field and β is the ratio of plasma pressure to magnetic pressure. It should be noted that with this sign convention, the initial background is in the $-\hat{z}$ direction, while the reversed field is in the $\hat{z}$ direction. The radial electric field is

$$E_r(r) = -r\omega_e B_z(r) - \frac{T_e}{e}\frac{d\ln[n_e(r)]}{dr} + \frac{m}{e}r\omega_e^2. \tag{6}$$

Although the electric field points away from the null surface, this radial acceleration is balanced by the $q\vec{v}\times\vec{B}$ term of the Lorentz force.

This model will be used to estimate the ion current in the laboratory frame. The unknown quantities B_0, β, r_0, and Δr are to be treated as free parameters in order to fit the model to the experimental data.

The two classes of particle orbits that arise from these fields are betatron and drift orbits. For electrons, the drift orbits travel in the direction of the plasma current while the betatron orbits are in the countercurrent direction. The betatron orbits for ions are in the cocurrent direction, and the drift orbits can be in either direction, depending on whether the $E\times B$ drift or the ∇B drift is dominating. These drifts will be considered as an explanation of the electron drift required to balance the ion flow in Sec. IV E.

For a plasma described by the rigid rotor distribution in Eq. (3), the ion contribution to the total plasma current in the laboratory frame can be found provided that the ion density profile $n_i(r,z)$ and the rotation frequency ω_i are known. The calculations in this section assume that the ion density only depends on radius over a length Δz. In equilibrium, the ion density's radial dependence for the 1D case is given by Eq. (4). The parameters r_0 and Δr can be estimated by fitting the theoretical magnetic field profile [Eq. (5)] to the experimental magnetic probe data with the free parameters B_0, β, r_0, and Δr. For the equilibrium model, B_0 refers to the applied magnetic field, which is not necessarily identical to the known initial background magnetic field from the limiter coil because some of the magnetic flux from this coil contributes to the trapped flux of the FRC. Not knowing exactly how much of this flux contributes is the motivation for treating B_0 as a free parameter. Since β is a function of B_0, it is also left as a free parameter.

Once r_0 and Δr are known, $n_i(r)$ can be radially integrated along the line of sight of the interferometer. Setting the resulting integral equal to the line integrated data will provide the normalization constant n_0, which is the peak density at r_0. Performing a fit to the magnetic probe data in Fig. 5 at $t=50$ μs, we find the parameter values to be $r_0=18$ cm and $\Delta r=7$ cm. A fit at 40 μs is shown in Fig. 14. With these parameters, the unnormalized density profile is integrated along the same chord viewed by the interferometer from Fig. 3(e) and the peak density at 40 μs is calculated to be 1.4×10^{15} cm^{-3}. The resulting density profile is shown in Fig. 15 along with the density computed from pressure balance in Sec. IV C and normalized ion saturation (I_{sat}) data from a Langmuir probe. The I_{sat} peaks have been normalized to be between the two distributions for a comparison of the shapes of the distributions. As shown, the rigid rotor equilibrium profile is narrower than what is measured by the Langmuir probe as well as what is calculated from pressure balance. The peak is also larger in the rigid rotor profile. This is expected since the interferometer (which is used for normalizing the rigid rotor profile) sees the actual profile, which is broader. Accordingly, the peak must be larger to account for the same line integrated density.

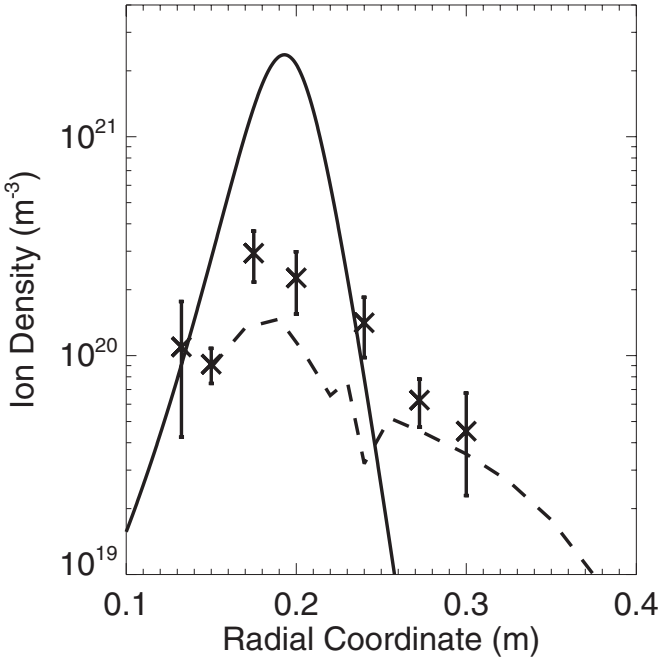

FIG. 15. Equilibrium density profile using fitted parameters (solid) during a stable portion of the discharge (t=60 μs) along with the profile calculated from pressure balance (dashed) and ion-saturation current ($\times$) scaled for reference.

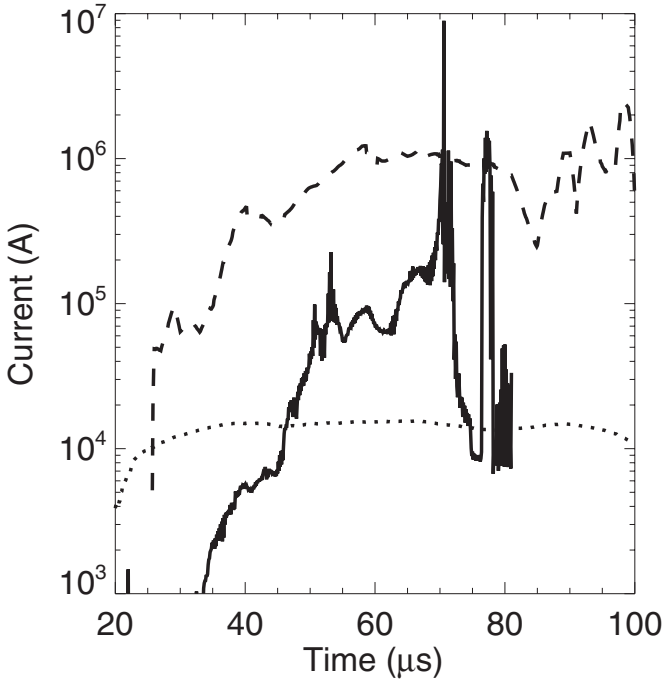

FIG. 16. Ion currents using density profiles obtained from pressure balance (dashed) and fitting to the equilibrium model (solid). Total plasma current shown (dotted) for comparison.

The axial extent of the plasma Δz is estimated by finding the axial length of the last closed flux surface. This is accomplished by calculating where the separatrix is in r as a function of the axial coordinate z. To determine where the separatrix is, the magnetic probe data from the radial array are integrated along r, and the net flux through a circle at radius r is calculated. Taking the flux along the outside of the flux coil to be zero, since the magnetic flux within the coil is not part of the trapped flux in the FRC, the separatrix is the radius at which the integral returns to zero. Δz is then the axial length between the points at which the separatrix radius is equal to the flux coil radius.

E. Plasma current

Plasma current is caused by the difference between the ion flow and the electron flow. The ion current in the laboratory frame is

$$I_i \simeq q\Delta z\omega_i \int n_i(r) r dr. \tag{7}$$

The ion rotation frequency ω_i is computed from the argon Doppler shift data in Fig. 10. Integrating the density profiles obtained from Secs. IV C and IV D gives the traces in Fig. 16. Although the peak density is higher for the fitted equilibrium density, the density profile from pressure balance integrates to a larger number since it is broader. From these current traces, it is observed that the ion contribution to the plasma current is at least an order of magnitude larger than the total current. Based on these findings, it must follow that the electrons are drifting in the same direction as the ions, resulting in a net current lower than the ion current

$$I_{\text{net}} = I_i - I_e. \tag{8}$$

The effect of neutrals on the ion and electron components has not been discussed in great detail primarily because the neutral density is not known on IFRC. Fortunately, the measurements that have been performed and the modeling of the current density do not rely and are not affected by the neutral density.

The laboratory frame contribution of the electrons to the current I_e can be estimated by finding the average drift velocity $\langle v_d \rangle$. The drift velocity for electrons is found by calculating the $E \times B$ and ∇B guiding center drifts. For $E_r(r)$ and $B_z(r)$ described in Sec. IV D, both of these drifts are in the direction of the plasma current, which effectively reduces the total plasma current. The average rotation frequency $\langle \omega_e \rangle$, which is related to v_d by $\langle \omega_e \rangle = \langle v_d / r \rangle$, is found by integrating over all possible drift velocities and scaling by the normalized density

$$\langle \omega_e \rangle = \frac{1}{\Delta r} \int_{r_{\min}}^{r_{\max}} \frac{n_e(r)}{n_0} \frac{v_d(r)}{r} dr. \tag{9}$$

The total current due to electrons and ions is

$$I_\theta = q(\omega_i - \omega_e) \int_{-\Delta z}^{\Delta z} \int_{r_{\min}}^{r_{\max}} n(r,z) r dr dz. \tag{10}$$

Using the measured total current, the different density profiles can be integrated to obtain an expected ω_e. These, along with $\langle \omega_e \rangle$ calculated from particle drifts, are shown in Fig. 17. The plotted range is restricted to the time in the discharge during which the FRC is the most stable (axial magnetic probes and plasma current are flat). As shown, the rotation

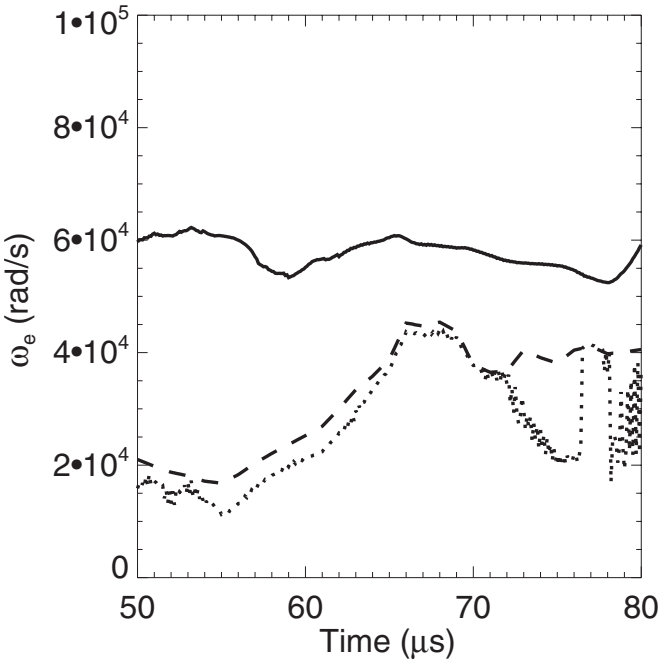

FIG. 17. Electron rotation frequencies calculated from particle drifts (solid) and using the integrated density distributions obtained from the equilibrium model fit (dotted) and pressure balance (dashed).

frequencies required to provide the measured plasma current are within an order of magnitude of the average rotation frequency calculated from the electron drift orbits.

V. CONCLUSIONS AND FUTURE WORK

Visible emission spectroscopy has been performed on various lines in IFRC. CII, ArII, and KrII show a Doppler shift resulting in a flow in the ion diamagnetic direction. Collisionality between the observed ions and the hydrogen plasma is high enough to assert that the hydrogen is rotating in the same direction. The flow of hydrogen is not observed through spectroscopy because most neutral emission occurs at the edge of the plasma, where there is little or no rotation. The neutral particle analyzer did not detect flow because the minimum detectable energy of the diagnostic is higher than the average drift.

Fitting a theoretical equilibrium to experimental data has allowed unknown parameters to be estimated. The ion current in the laboratory frame is between one and two orders of magnitude higher than the measured total plasma current. The electron rotation frequency necessary to reduce the ion current to the level of the measured total current is within a factor of 3 of the rotation frequency calculated from the drift orbits estimated from the equilibrium fields.

The analysis performed in this paper is heavily dependent on the plasma being a rigid rotor distribution and knowing the plasma density profile. Further verification of the findings requires more measurements of the density profile both radially and along the axis of the FRC. Additionally, local measurements of the plasma flow can test the validity of the rigid rotor model for IFRC. A gridded energy analyzer is presently in development for this purpose. The electron drifts have been calculated using the theoretical radial electric field. Measurements of the radial electric field are needed to confirm these estimates.

ACKNOWLEDGMENTS

The authors thank Justin Little for his work with the early stages of the spectrometer; F. Brandi, F. Giammanco, and E. Paganini for the implementation and analysis of the second harmonic interferometer.

[1] M. Tuszewski, Nucl. Fusion **28**, 2033 (1988).
[2] M. W. Binderbauer and N. Rostoker, J. Plasma Phys. **56**, 451 (1996).
[3] J. M. Finn and R. N. Sudan, Nucl. Fusion **22**, 1443 (1982).
[4] R. E. Siemon, W. T. Armstrong, D. C. Barnes, R. R. Bartsch, R. E. Chrien, J. C. Cochrane, W. N. Hugrass, R. W. Kewish, P. L. Klingner, H. R. Lewis, R. K. Linford, K. F. McKenna, R. D. Milroy, D. J. Rej, J. L. Schwarzmeier, C. E. Seyler, E. G. Sherwood, R. L. Spencer, and M. Tuszewski, Fusion Technol. **9**, 13 (1986).
[5] Y. Ito, N. Arai, Y. Ueda, A. Sugimoto, S. Okada, S. Goto, and T. Ishimura, Jpn. J. Appl. Phys., Part 1 **30**, 1475 (1991).
[6] Y. Ono, T. Matsuyama, K. Umeda, and E. Kawamori, Nucl. Fusion **43**, 649 (2003).
[7] C. D. Cothran, J. Fung, M. R. Brown, M. J. Schaffer, and E. Belova, J. Fusion Energy **26**, 37 (2007).
[8] F. Brandi and F. Giammanco, Opt. Lett. **33**, 2071 (2008).
[9] Z. A. Pietrzyk, G. C. Vlases, R. D. Brooks, K. D. Hahn, and R. Raman, Nucl. Fusion **27**, 1478 (1987).
[10] W. S. Harris, E. P. Garate, W. W. Heidbrink, R. McWilliams, T. Roche, E. Trask, and Y. Zhang, Rev. Sci. Instrum. **79**, 10F313 (2008).
[11] A. S. Alhasi and J. A. Elliot, Plasma Phys. Controlled Fusion **34**, 947 (1992).
[12] J. D. Huba, *NRL Plasma Formulary* (Naval Research Laboratory, Washington, DC, 2007).
[13] R. J. Goldston and P. H. Rutherford, *Introduction to Plasma Physics* (Institute of Physics, University of Reading, Berkshire, 2000), p. 151.
[14] D. J. Rej and W. T. Armstrong, Nucl. Fusion **24**, 117 (1984).
[15] N. Rostoker and A. Qerushi, Phys. Plasmas **9**, 3057 (2002).